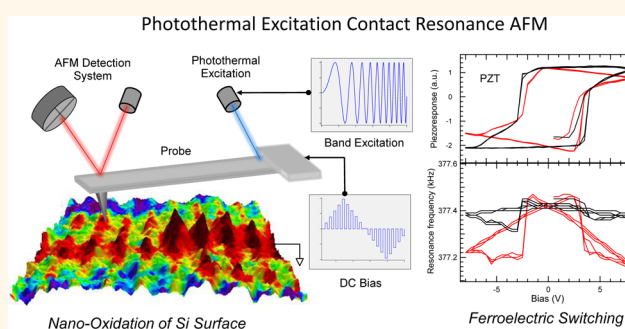


Probing Local Bias-Induced Transitions Using Photothermal Excitation Contact Resonance Atomic Force Microscopy and Voltage Spectroscopy

Qian Li,[†] Stephen Jesse,[†] Alexander Tselev,[†] Liam Collins,[‡] Pu Yu,[§] Ivan Kravchenko,[†] Sergei V. Kalinin,[†] and Nina Balke^{*,†}

[†]Center for Nanophase Materials Sciences, Oak Ridge National Laboratory, Oak Ridge, Tennessee 37831, United States, [‡]School of Physics, University College Dublin, Belfield, Dublin 4, Ireland, and [§]State Key Laboratory for Low-Dimensional Quantum Physics, Department of Physics, Tsinghua University, Beijing 100084, China

ABSTRACT Nanomechanical properties are closely related to the states of matter, including chemical composition, crystal structure, mesoscopic domain configuration, etc. Investigation of these properties at the nanoscale requires not only static imaging methods, e.g., contact resonance atomic force microscopy (CR-AFM), but also spectroscopic methods capable of revealing their dependence on various external stimuli. Here we demonstrate the voltage spectroscopy of CR-AFM, which was realized by combining photothermal excitation (as opposed to the conventional piezoacoustic excitation method) with the band excitation technique. We applied this spectroscopy to explore local bias-induced phenomena ranging from purely physical to surface electromechanical and electrochemical processes. Our measurements show that the changes in the surface properties associated with these bias-induced transitions can be accurately assessed in a fast and dynamic manner, using resonance frequency as a signature. With many of the advantages offered by photothermal excitation, contact resonance voltage spectroscopy not only is expected to find applications in a broader field of nanoscience but also will provide a basis for future development of other nanoscale elastic spectroscopies.



KEYWORDS: scanning probe microscopy · elastic spectroscopy · Young's modulus · ferroelectric · electrochemical reaction

Atomic force microscopy (AFM) comprises a wide family of modalities that are developed to probe various aspects of physical and chemical properties of materials.¹ Mechanical properties are of great importance for any materials, and obtaining a full understanding of them requires information down to the nanoscale. Several nanomechanical AFM techniques exist that operate in different regimes of the tip–sample interaction, e.g., tip indentation (force–distance spectroscopy),² intermittent-contact frequency modulation AFM,³ and contact resonance AFM (CR-AFM).⁴ Typically in CR-AFM, the tip is excited at its resonance frequencies with a piezoelectric transducer, either attached underneath to the samples (this variant is called

atomic force acoustic microscopy, AFAM^{5,6}) or directly coupled with the cantilever (called ultrasonic atomic force microscopy, UAFM⁷). With the advantages of resonance enhancement, local elastic properties of samples can be detected with high sensitivity and large dynamic range in CR-AFM, leading to its applications in diverse materials ranging from polymers⁸ to minerals⁹ and to biological samples.¹⁰ A major technical issue in the development of CR-AFM is to obtain a clean, broadband, and versatile excitation manner. Although piezoacoustic excitation is the current method of choice, it has some shortcomings, such as noises and spurious coupling effects. The latter effect is especially severe in liquid environment. Attempts to operate CR-AFM in liquid were

* Address correspondence to balken@ornl.gov.

Received for review November 26, 2014 and accepted January 5, 2015.

Published online January 05, 2015
10.1021/nn506753u

© 2015 American Chemical Society

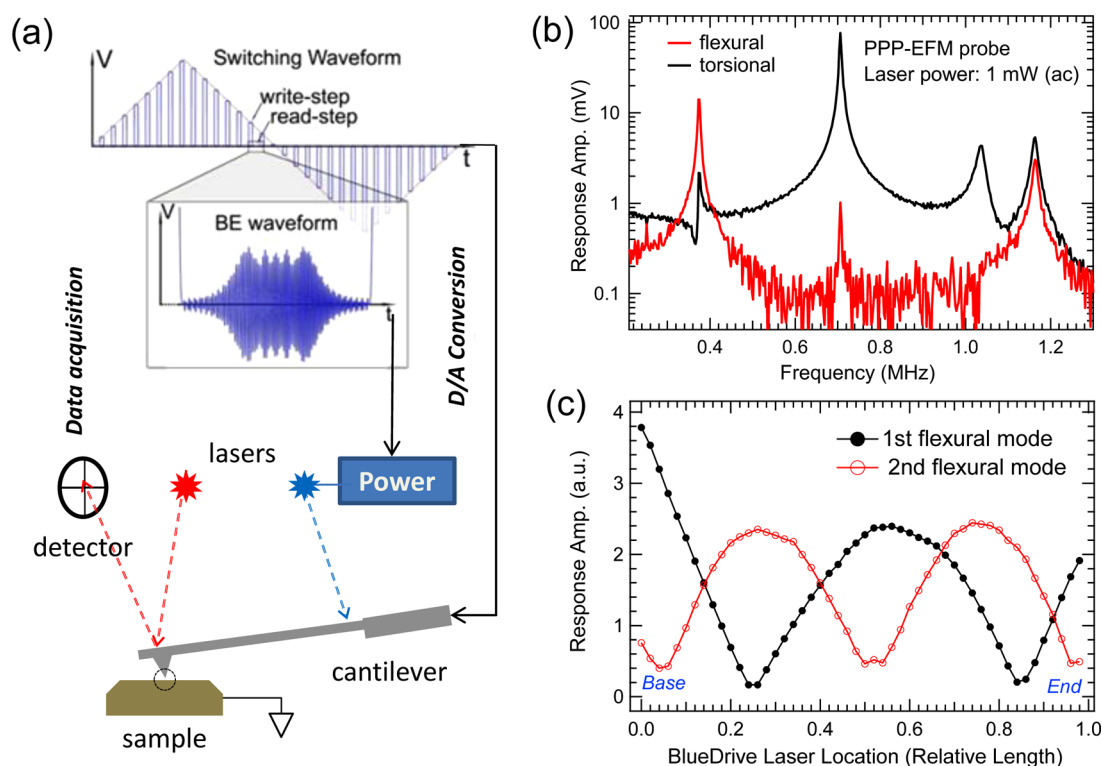


Figure 1. (a) Schematic of photothermal excitation CR-AFM in combination with BE voltage spectroscopy. (b) Typical amplitude versus frequency response spectra in flexural and torsional modes, acquired from the vertical and lateral channels of the detector, respectively. (c) Amplitude of the first and second flexural modes as a function of BlueDrive laser location on the cantilever (sample: Si substrate).

only made possible by using magnetic (Lorentzian force) excitation, which however requires specially prepared tips, thus limiting its applications.¹¹ Photothermal excitation is another type of non-contact coupling actuation method, which has been frequently demonstrated for topography imaging, with particular interests in imaging in liquid, since the earliest days of AFM.^{12,13} Here, we explore the use of photothermal excitation, recently available from a commercial “BlueDrive” module,^{14,15} in CR-AFM.

On the other hand, spectroscopic modes of CR-AFM have been largely missing so far. This thus limits CR-AFM to static imaging measurements, in contrast to many other AFM modalities. For example, the switching spectroscopy of piezoresponse force microscopy (PFM) is now a standard technique for studying nanoscale ferroelectric domain switching dynamics,¹⁶ and its counterparts in Kelvin probe force microscopy are also developed to probe surface charge dynamics under tip biasing.^{17,18} Previously, Nikiforov *et al.* incorporated localized tip heating into AFAM and enabled dynamic probing of temperature induced phase transitions.¹⁹ In this work, we have implemented contact resonance voltage spectroscopy, based on our existing set of band excitation (BE) spectroscopies. The BE method not only provides the flexibility in signal generation and acquisition essential for realizing the measurement protocols but also achieves unparalleled

accuracy in capturing and recovering the full tip–sample interaction information.^{20–22} In conjunction with photothermal excitation, this spectroscopic method has enabled us to probe the bias-induced dynamic processes of ferroelectric domain switching and local irreversible electrochemical reactions. The obtained results demonstrate that those tip bias-induced minute changes in the surface properties, either local elastic moduli or morphology, can be sensitively traced from contact resonance spectroscopy.

RESULTS AND DISCUSSION

Photothermal Excitation CR-AFM. Figure 1a shows a schematic of BE contact resonance voltage spectroscopy. This method is similar to PFM switching spectroscopy in that we use dc voltage pulses to induce changes in the sample surface states (*i.e.*, domains in ferroelectrics) and probe such changes with ac/BE signals during and/or after dc pulses. The main modification here is that BE signals are routed to the BlueDrive modulation circuit instead of being applied to the cantilever. In our scheme, we use two analog outputs in the PXI-6124 card to synchronously generate BE and dc waveforms that are digitally constructed from a set of parameters, *e.g.*, bandwidth/amplitude and pulse length. Note that only a triangular dc step waveform has been implemented in this work; however, more complex measurement protocols such as

first-order reversal curve,²³ ac amplitude sweeping,²⁴ and time-domain relaxation curve²⁵ can be combined with contact resonance spectroscopy. On receiving each BE waveform, the cantilever starts to oscillate at the chosen band of frequencies as photothermally excited. The time domain responses of the cantilever in contact with a sample are acquired over the same time length and then Fourier transformed into frequency domain response spectra, which contain the tip–sample interaction information. The damped harmonic oscillator (DHO) model is usually used to describe a contact resonance frequency spectrum, which has amplitude/phase forms as

$$A(f) = \frac{f_0^2 A_{\text{drive}}}{\sqrt{(f_0^2 - f^2)^2 + (f_0 f / Q)^2}} \quad (1a)$$

$$\varphi(f) = \tan^{-1} \left(\frac{f_0 f}{Q(f_0^2 - f^2)} \right) + \varphi_{\text{drive}} \quad (1b)$$

where f_0 is the resonance frequency and Q the quality factor; A_{drive} and φ_{drive} are the amplitude and phase, respectively, of the driving force. The use of BE allows highly accurate decoupling of these DHO parameters, since the cantilever response spectra are sampled with many frequency points with intervals equal to the reciprocal length of each BE waveform.²⁰ In addition to BE, we also used the dual ac resonance tracking (DART) method in this study, especially for imaging modes. DART enables faster imaging speeds but only measures the response at two frequency points, which nonetheless are sufficient to solve the DHO model parameters despite inferior accuracy to the BE method.^{26,27}

Figure 1b shows typical measured flexural/vertical and torsional/lateral mode resonance spectra for a single probe, obtained with 1 mW oscillation laser power. In this example, the excitation laser spot was placed near the cantilever base and slightly shifted aside for excitation of torsional modes. As can be seen, both the flexural and torsional spectra are clean with very weak crosstalk between them and the peak shape of all modes agrees well with an ideal DHO model, demonstrating the effectiveness of photothermal excitation as well as its selective property. Obviously, this can be an important advantage compared to piezoacoustic actuation (for both the cases of AFAM and UAFM). The latter usually cannot excite both vertical and in-plane displacements of a sample efficiently with a single transducer and sample configuration.²⁸ Besides, we found that the excitation efficiency is uniquely determined for each flexural mode by the excitation laser locations on cantilevers. As illustrated in Figure 1c, during the blue laser spot scanning from the cantilever base to its end (meanwhile the detection laser was fixed at the end), the amplitude of the first and second modes varies in an anti-correlated manner,

and in both cases it shows a profile reminiscent of cantilever mode shapes. In fact, these results reveal the length profiles of local stress gradient associated with each mode shape. The maximum stress gradient point is near the cantilever base for the first mode. Except that, all other (local) maxima coincide with the largest displacement points in the respective mode shapes. Such a measurement not only provides an experimental guide for choosing proper excitation locations, but we further point out that, it can be used to study the mode shapes, which are significantly dependent on the tip–sample contact stiffness, k^* .

Quantitative Data Analysis in CR-AFM. As a standard procedure in AFAM/UAFM, one first derives the contact stiffness from measured resonance frequencies and associated Q factors of the contact resonance peaks, using cantilever dynamics models that can be solved analytically or using numerical methods. Generally, a linear Euler–Bernoulli beam is adopted to model the cantilever, and the tip–sample elastic interaction is approximated as a spring in parallel with a dashpot (*i.e.*, Kelvin–Voigt model; see Figure 2a), if only the vertical coupling is considered.^{5–7,29,30} Here, the spring represents the contact stiffness, whereas the dashpot accounts for the material damping behavior (also called viscoelasticity). We solved these models numerically based on the mathematic formalism of Rabe,⁶ in particular, we have considered both the vertical and lateral contact coupling. Figure 2b presents the calculated results for typical PPP-EFM cantilevers that were used for this study. As can be seen, the resonance frequency rises as the contact stiffness increases, but meanwhile its sensitivity (first derivative) decreases monotonically. On the other hand, the Q factor, calculated for a given material damping factor, has a complex dependence that first increases and then decreases with contact stiffness. In our experiment range ($k^* \approx 400\text{--}700$ N/m), the Q factor shows a relatively flat trend and hence it is well justified to attribute the observed Q variations directly to changes in the viscoelastic properties of materials.

Having quantified the contact stiffness, one is then enabled to calculate elastic moduli of the samples based on contact mechanics models. The prevailing model used in the field is the Hertzian model, which, in a general sense, relates contact stiffness with contact radius a_c and reduced Young's modulus E^* as $k^* = 2a_c E^*$. Among them, the reduced Young's modulus of the contact is defined as

$$\frac{1}{E^*} = \frac{1 - \nu_s^2}{E_s} + \frac{1 - \nu_T^2}{E_T} \quad (2)$$

where ν_s , ν_T , and E_s , E_T are the Poisson ratios and Young's moduli of the sample surface and AFM tip, respectively. The contact radius is determined by the tip shape and applied loading force. In practice, however, a calibration approach is mostly followed to

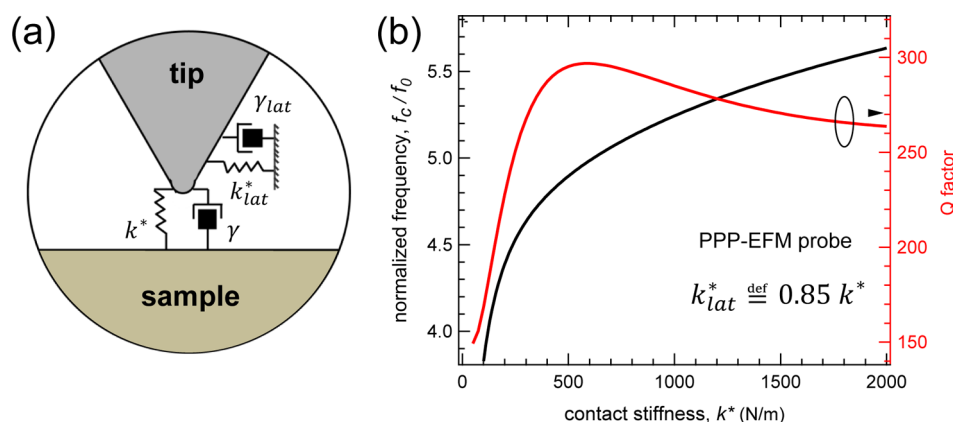


Figure 2. (a) Schematic of the tip–sample elastic interaction. (b) First flexural mode contact resonance frequency (normalized to the free frequency) and Q factor as a function of contact stiffness, calculated for PPP-EFM probes on the basis of their nominal geometric parameters. A constant material damping coefficient was used to calculate the Q factors.

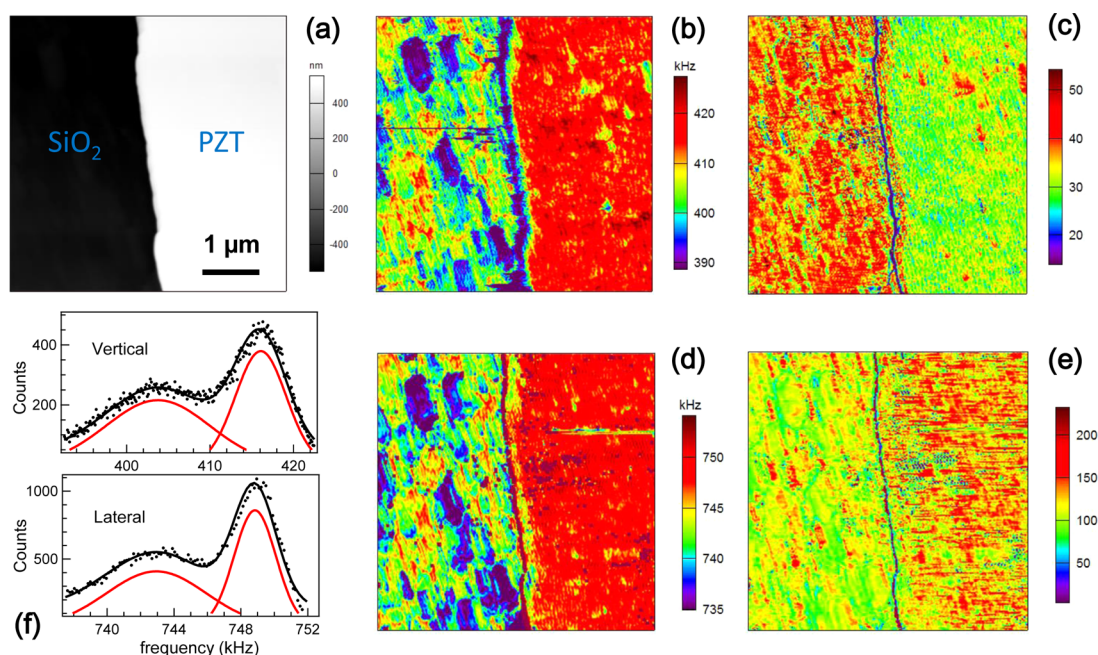


Figure 3. (a) Topography of PZT/SiO₂ boundary. (b,d) Resonance frequency and (c,e) Q factor of the (b,c) vertical and (d,e) torsional mode photothermal excitation CR-AFM of the boundary region. (f) Histogram of the resonance frequency data and their fits by Gaussian peaks.

circumvent direct quantification of the contact radius. That is, the results obtained on the unknown sample and a (or multiple) reference sample with known elastic moduli are compared according to the relation:

$$E^* = E_{\text{Ref}}^* (k^*/k_{\text{Ref}}^*)^m \quad (3)$$

where E_{Ref}^* and k_{Ref}^* are the reduced Young's modulus and measured contact stiffness of the reference sample, respectively; $m = 1.5$ for the case of spherical tip shape and $m = 1$ when the tip is a flat punch. A previous study showed that the tip shapes are prone to acquire a flat punch shape after initial few “break-in” contact measurements.³¹

Applications of CR-AFM/Voltage Spectroscopy. In the following part, we first present an example of photothermal

excitation CR-AFM imaging measurement which reveals clear mechanical property contrast on dissimilar materials. Then we show the results of contact resonance switching spectroscopy obtained on typical ferroelectric materials and compare them with the PFM switching spectroscopy results. Finally, an example is presented in which contact resonance voltage spectroscopy is applied to probe local irreversible electrochemical reactions.

Figure 3a shows the topography of the sputtered PZT thin film across the PZT/SiO₂ boundary. Both the PZT and SiO₂ layers show polycrystalline morphology and the latter is somewhat rougher (see Figure S1). This morphology is not well shown in the height image due to its large scale ($\sim 1 \mu\text{m}$). These two layers of different

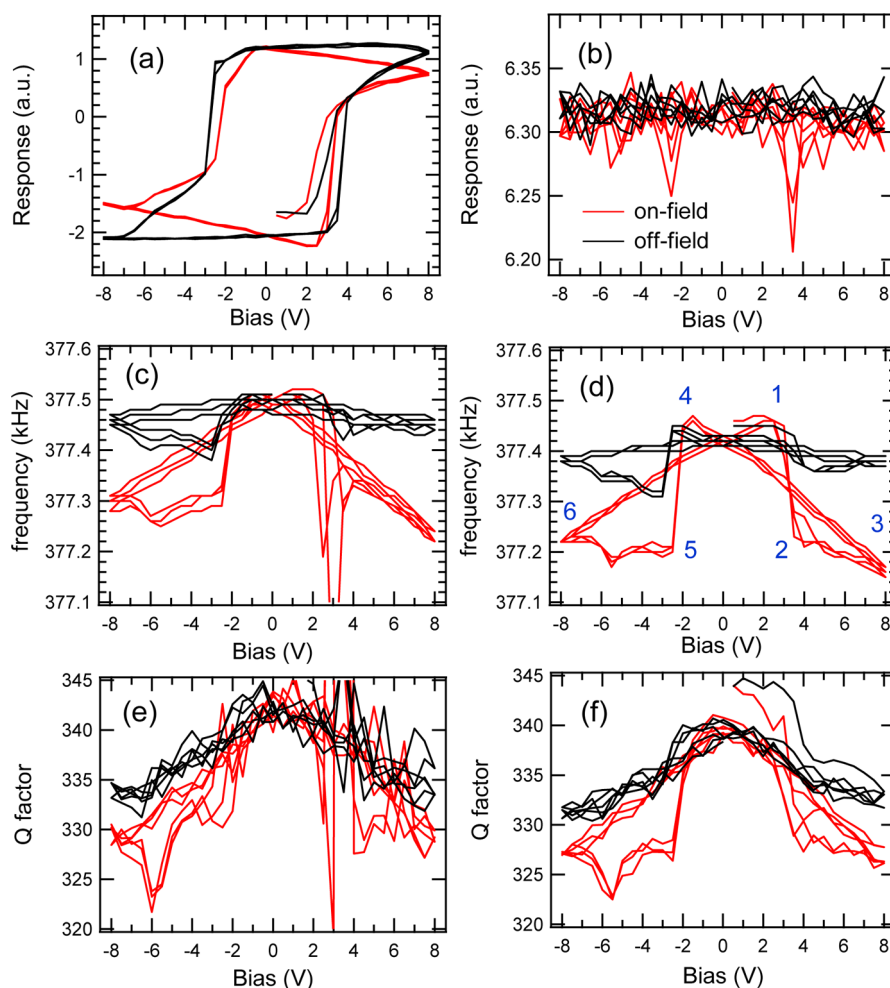


Figure 4. Single-point (a,b) amplitude, (c,d) resonance frequency, and (e,f) Q factor loops of (a,c,e) piezoresponse and (b,d,f) photothermal excitation contact resonance switching spectroscopy, measured on 100 nm epitaxial PZT thin film.

materials show clear difference in vertical contact resonance frequency, as shown in Figure 3b. Fitting to the histogram of the frequency image (Figure 3f) reveals that $f_{C,Vert.} = 416.1 \pm 4.3$ kHz for PZT and 403.8 ± 8.8 kHz for SiO_2 . The frequency distribution of the SiO_2 layer is much broader, due to the presence of a few grains that appear softer (showing lower frequencies) and also inclusion of the boundary regions. Using SiO_2 (Young's modulus: 70 GPa) as an internal calibration material and following the procedure described before, we obtain the Young's modulus for PZT as 125 ± 15 GPa. This value is in reasonable agreement with the reported values for similar polycrystalline PZT thin films, *e.g.*, 110 GPa from ref 32. In comparison with the resonance frequency, the Q factor image shows an opposite contrast (Figure 3c). An average $Q \approx 38$ is measured for SiO_2 , slightly higher than that ($Q \approx 32$) for PZT. Since the Q factor is mainly associated with energy dissipation in the tip–sample elastic interaction, this contrast may suggest a higher structural integrity of the SiO_2 layer as a result of the growth process. On the other hand, the PZT film also appears stiffer than SiO_2 from the torsional mode measurement results

(Figure 3d) and their resonance frequency are found to be $f_{C,Tor.} = 748.8 \pm 1.8$ and 743.0 ± 4.2 kHz, respectively (Figure 3f). The Q factor image (Figure 3e) in this case shows the same contrast as the frequency image albeit the difference is again small (average value $Q \approx 130$ for PZT and 110 for SiO_2). The torsional mode contact stiffness is associated with the shear modulus of samples and can be quantitatively analyzed in a similar way to derive the modulus values.²⁸ However, this analysis goes beyond the scope of the present work.

Figure 4 shows a typical set of piezoresponse and contact resonance switching loops measured sequentially on the same location on 100 nm epitaxial PZT thin film. This sample has a homogeneous, upward-polarized single domain state without detectable in-plane domain structures as known from PFM imaging, and the CR-AFM imaging results also show little contrast (see Figures S2 and S3). Therefore, the domain switching process here is 180° reversal of the polarization vector. As illustrated in Figure 4a, canonical square piezoresponse loops are measured over the film surface suggesting its high epitaxial quality (the on-field loops are distorted due to the accompanying

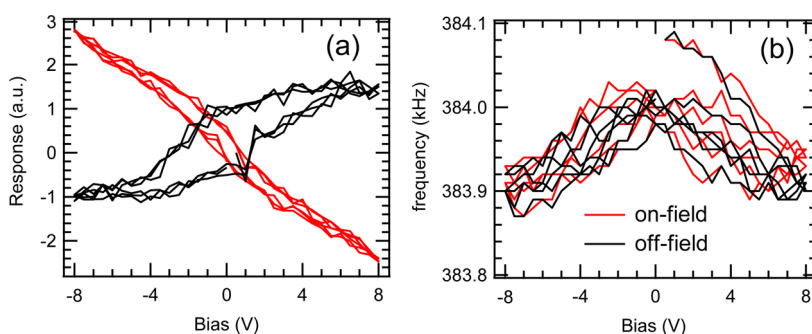


Figure 5. (a) Electrostatic response hysteresis loops and (b) photothermal excitation contact resonance frequency loops, measured at the same location on amorphous HfO_2 thin film. The on-field loops in (a) are divided by a factor of 2.

electrostatics response). Overall, the resonance frequency and Q factor loops of the piezoresponse spectroscopy shows excellent consistency with the contact resonance spectroscopy results. The former loops are somewhat noisier, especially near switching voltages where the piezoresponse is inherently low. In contrast to this type of self-actuation in PFM, photothermal excitation provides almost constant amplitude/phase actuation during the domain switching process (cf. Figure 4a,b), and this advantage becomes increasingly important when the studied materials have weaker piezoelectric properties that cannot excite the contact resonances to an appreciable level themselves. Therefore, coupled with the BE method, photothermal excitation contact resonance spectroscopy can achieve extremely accurate assessment of minute changes in the sample elastic properties.

Looking closely at the on-field frequency loops (Figure 4d), it is apparent that the largest frequency shift, an abrupt decrease by ~ 240 Hz, occurs at the anti-parallel domain nucleation stages (*i.e.*, Stages 1-2 and 4-5),³³ concurrent with a decrease of the Q factor, indicating local softening and increased internal friction loss of the material. At the domain growth stages, there is a subtle but stable (among a few cycles) difference between the positive and negative sides; Stage 2-3 shows a slowly decreasing trend while Stage 5-6 is relatively stable. This could reflect their different domain configurations in connection with the upward domain matrix of the film. Finally, decreasing tip voltages after domain saturation (Stages 6-1 and 3-4) results in constant rate recovering of the resonance frequency. On the other hand, the off-field frequency loops do not match the on-field ones entirely and their frequency shifts are generally smaller, implying that the observed softening/recovering effect is not only domain structure-related but has a large content of lattice origins. For ferroelectric materials, it is easy to perceive that domain walls can have different mechanical properties from the crystal matrix since they are, essentially, structural defects; besides, domains per se are mechanically anisotropic with respect to the polarization directions. Tsuji *et al.* observed 10%

lower contact stiffness on domain walls in bulk PZT samples using UAFM imaging.³⁴ We further note that a recent macroscopic study found over 30% change of the Young's modulus of PZT ceramics during polarization hysteresis loop measurements.³⁵ In our case, the contact stiffness variations during the switching cycles are found to be rather small (less than 1%). This can be certainly because our measurement is dynamic and domain switching occurs in a rather localized volume. More importantly, it may point to the fact that the switching process in the PZT thin film is purely 180° with no occurrence of ferroelastic domain walls which alters elastic properties of materials more effectively. In light of this analysis, we argue that the frequency shift can be a reliable signature for identifying true ferroelectric domain switching processes, whether of a 180° or non- 180° type, and thus contact resonance switching spectroscopy can be combined with PFM to explore unknown materials and avoid possible misinterpretations.

Recently, we found that well-defined off-field response hysteresis loops with clear 180° phase flips, closely resembling those usually observed on ferroelectric materials, are measured on amorphous HfO_2 thin film; however, these loops by no means suggest ferroelectricity of the material and instead they can be ascribed to hysteretic electrostatic responses due to local charge injection and dissipation.¹⁸ A selected example of such loops, along with the resonance frequency loops obtained at the same location using photothermal excitation, are presented in Figure 5. In contrast to real PFM response, no frequency anomalies are observed near the "switching" voltages in this case and little difference exists between the on and off field loops. The small, hysteresis-free frequency shift thereof may originate from certain types of bias-induced surface state changes in amorphous HfO_2 except for domain switching.

The nanoscale oxidation phenomena of silicon have been extensively explored in the context of scanning probe nanolithography.^{36–38} In this process, negative biases are applied to an AFM tip (thus Si substrate is the anode) which is placed in contact with or very close to

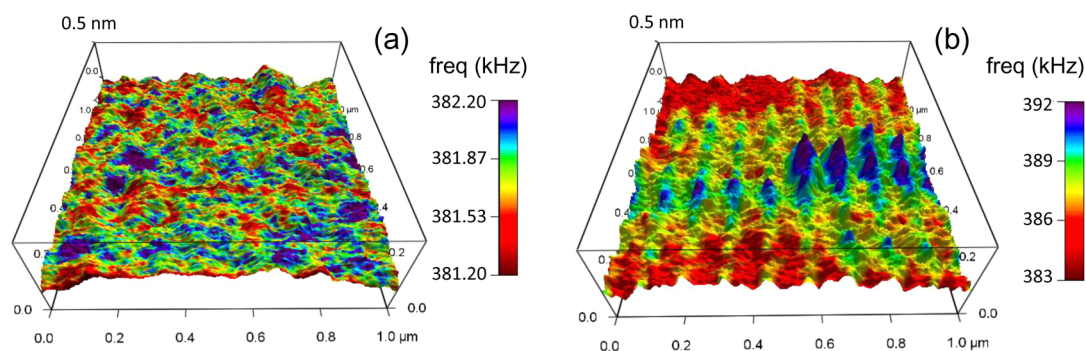


Figure 6. 3D topography of a $1 \times 1 \mu\text{m}^2$ region on Si(001) substrate overlaid with corresponding CR-AFM frequency images, (a) before and (b) after the voltage spectroscopy measurement performed on a 10×10 grid.

the Si surface, and then the water meniscus surrounding the tip–sample junction is decomposed by electrons injected from the biased tip, *i.e.*, $2\text{H}_2\text{O} + 2\text{e}^- \rightarrow \text{H}_2\uparrow + 2\text{OH}^-$. The resultant hydroxyl ions further react with the Si substrate and thereby SiO_2 forms on the surface. This is typically an irreversible electrochemical process, and controlled by a number of factors, *e.g.*, bias voltage/duration and humidity. Static measurements of the height/size of formed SiO_2 nanostructures were predominately used in previous studies to study the reaction kinetics in regard to those factors. Furthermore, tip bias-induced electrochemical reactions are also observed on some other oxides surface, for example, CeO_2 ³⁹ and Li-ion electrolytes (reduction of Li^+).^{23,40} In these studies, current measurements and real-time height monitoring/control were also implemented, yielding wealthy information about the reaction kinetics thereof.

Here, we applied contact resonance voltage spectroscopy to probe the Si nano-oxidation process. Three consecutive cycles of dc waveforms [± 8 V bias window, total length = 4 ms (per step) \times 64 (steps) \times 2 (on/off-field)] were applied at 10×10 locations evenly defined on a $1 \times 1 \mu\text{m}^2$ surface region. As shown in Figure 6a, the pristine surface is extremely smooth (rms roughness ~ 0.05 nm) and shows a small frequency variation ~ 235 Hz across the scanned area, both pertaining to the quality of the substrate used. After the spectroscopy measurement, mild changes occur to the topography with only a few SiO_2 dots clearly discernible, the highest dot being ~ 0.4 nm (lateral size ~ 80 nm; see Figure 6 b). This means that the applied biases only induced an early growth stage of the oxidation process. By contrast, changes in the resonance frequency image are more apparent and the largest changes up to ~ 10 kHz (corresponding to $\sim 30\%$ increase of contact stiffness) are observed on the highest SiO_2 dots (see also Figure 7b. Inset). Figure 7a shows the amplitude spectrograph for a typical location, which captured the entire reaction process at this site. As shown in Figure 7a, the frequency does not change during the first half (positive) cycle until the bias reaches a negative value ~ -2 to -3 V. This threshold voltage is reasonably close to the H_2O

electrolysis potential (-1.23 V) given the likely existence of a potential drop at the tip–sample junction⁴¹ and other overpotential factors. Above this threshold, the frequency increases quickly with bias ramping to the maximum negative value in a nearly sigmoidal way that suggests the voltage dependent kinetics of the local reaction (Figure 7b). Then during the last quarter of the loop and following repeats of the same dc waveform, the frequency varies slowly, yet still in some characteristic ways. Compared with the frequency loops, the Q factor loops appear similar overall, a remarkable difference lying at the first negative half cycle where Q appears unchanged or even slightly reduced. For both of them, the on- and off-field loops overlap well with each other, indicating a stable remnant state after each dc pulse.

The explanation of the observed frequency shifts is not straightforward. Since SiO_2 has a much smaller Young's modulus than Si (160 GPa), the contact stiffness might be expected to become smaller after SiO_2 forms in between the tip–Si interface. Therefore, on contrary to our observations, the resonance frequency would decrease if the contact area is unchanged.⁴² However, one has to realize that the local stress field exerted by the tip can extend into the sub-surface with a depth of, as a rule of thumb, 3 times of the contact radius (~ 10 nm in this case).⁶ This depth is much higher than the formed SiO_2 dot (~ 0.4 nm) and thus the probed volume remains largely unmodified. Again, assuming a constant contact area, the Young's modulus is calculated to be ~ 220 GPa for the 10 kHz frequency shift. Such a sizable material hardening effect seems very unlikely to be true for Si. From the above analysis, the most reasonable explanation is the variation of contact area during the oxidation process. Stan *et al.* considered the influence of topography on contact area in a study on granular Au film, and proposed the concept of single/multiple-asperity contact.⁴³ A multiple-asperity contact enlarges the contact area and seems to fit the scenario here because SiO_2 nucleates around the biased tip and may change local curvatures of the surface. Despite the origin of the frequency shift, it provides a very sensitive

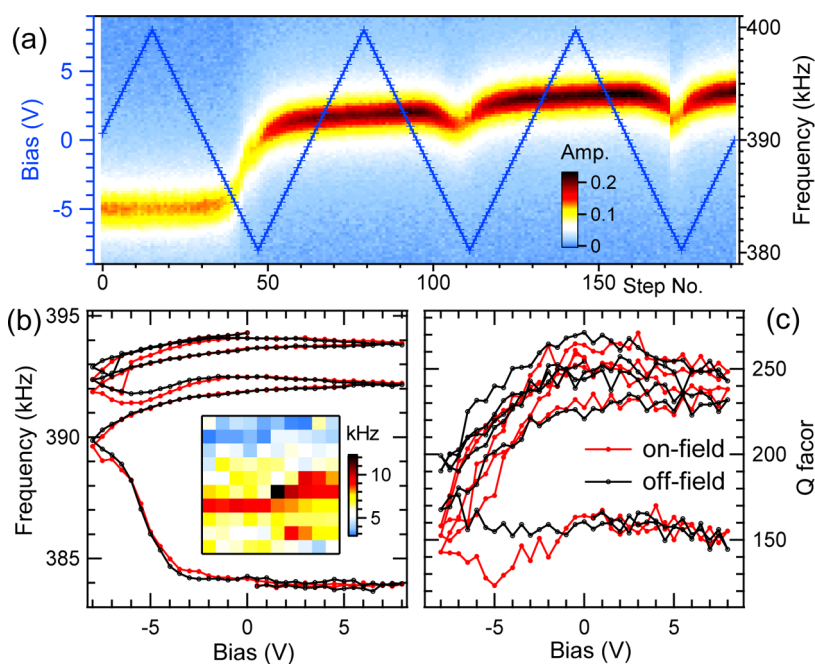


Figure 7. (a) Amplitude spectrograph at a selected location with the dc waveform overlaid. (b) Resonance frequency and (c) Q factor loops extracted from the data in (a). Inset in (b) is the frequency shift map for the measured grid.

measure of the onset and progress of the electrochemical reaction.

SUMMARY

We have explored the use of photothermal excitation in CR-AFM and developed its voltage spectroscopy based on the BE method. It is shown that photothermally excited CR-AFM produces well-defined material contrast between PZT/SiO₂, and their elastic moduli can be obtained from a quantitative analysis. The spectroscopic measurements on an epitaxial PZT thin film reveal small but well detectable stiffness changes during local polarization switching processes. Such changes appear to be characteristic of ferroelectric materials and thus can be a criterion for distinguishing the presence of domain switching in materials with unknown ferroelectric properties, which was demonstrated on

HfO₂ as an example for a non-ferroelectric material. We have also studied Si nano-oxidation phenomena using the voltage spectroscopy. The results show that the contact resonance frequency shifts remarkably during an early stage of the reaction when the morphology of the SiO₂ product is still not well developed. This suggests the high sensitivity of contact resonance voltage spectroscopy in detection of local irreversible electrochemical processes. Extending from this work, more CR-AFM spectroscopic methods can be envisaged for probing the nanomechanical behavior of materials under other types of applied stimuli. Finally, we emphasize that contact resonance spectroscopy in principle can also be implemented using alternative excitation manners coupled with other multifrequency AFM techniques that are capable of robust resonance frequency tracking and provide quantitative dissipation information as well.

METHODS

Experiment and Sample Details. All AFM measurements were carried out under ambient environment on a commercial AFM (Cypher, Asylum Research) equipped with a BlueDrive photothermal excitation module. A home-built BE system based on a NI (National Instruments) PXI-6124 data acquisition/analog output card was integrated with the microscope in Labview software environment. Pt/Ir-coated conductive Si probes, Nano-sensor PPP-EFM, were used, which typically have a moderate stiffness of 4–5 N/m and resonance frequency of 75–80 kHz as experimentally found. The set point force was maintained at ~350 nN for all contact-mode measurements. Several different types of samples were investigated, including a 1 μm Pb(Zr,Ti)O₃(PZT)/Pt/SiO₂ polycrystalline thin film deposited with sputtering techniques (this sample has shape boundaries between the PZT and SiO₂ layers), a 100 nm PZT thin film epitaxially grown on SrRuO₃(001) SrTiO₃ with pulsed laser deposition, a

10 nm amorphous HfO₂ film grown on Si(100) with atomic layer deposition, and a commercial n-doped Si(001) substrate. The samples were directly glued with silver paint on metal sample pucks which sat on the AFM scanner and were grounded.

The BlueDrive Module. BlueDrive employs a blue laser beam (wavelength $\lambda = 405$ nm) that is focused and transmitted to the cantilever through the same objective as the infrared laser beam used for optical lever detection. The optical system is designed in such a way that the blue laser beam can be independently moved along or perpendicular to the cantilever within certain travel ranges. Therefore, both laser beams can be aligned onto proper positions of the cantilever. When exposed to the blue laser beam, the cantilever is locally heated and thermal strain occurs to the laser spot location thereby actuating the cantilever. To oscillate the cantilevers, the blue laser power is modulated with a required dynamic signal. For most cases, the oscillation power level needs to be set below certain

limits to ensure linear response of cantilevers, typically a few milliwatts in this work. The BlueDrive module allows for high speed (up to 6 MHz), large dynamic range modulation, and user-configurable signal routing. These features have made our implementation of BE contact resonance voltage spectroscopy feasible.

Conflict of Interest: The authors declare no competing financial interest.

Acknowledgment. Personal support was provided by the U.S. Department of Energy, Office of Basic Energy Sciences, Materials Sciences and Engineering Division, through the Office of Science Early Career Research Program (N.B., Q.L.). The experiments were performed at the Center for Nanophase Materials Sciences, which is sponsored at Oak Ridge National Laboratory by the Scientific User Facilities Division, Office of Basic Energy Sciences, U.S. Department of Energy, which also provided additional personal support (S.J., A.T., S.V.K.).

Supporting Information Available: Some details of the cantilever dynamics model and PFM/CR-AFM imaging results of the sputtered PZT/SiO₂ thin film and epitaxial PZT/STO thin film samples. This material is available free of charge via the Internet at <http://pubs.acs.org>.

REFERENCES AND NOTES

1. *Scanning Probe microscopy of Functional Materials*; Kalinin, S. V., Gruverman, A., Eds.; Springer: New York, 2010.
2. Cappella, B.; Dietler, G. Force-Distance Curves by Atomic Force Microscopy. *Surf. Sci. Rep.* **1999**, *34*, 1–104.
3. Proksch, R.; Yablon, D. G. Loss Tangent Imaging: Theory and Simulations of Repulsive-Mode Tapping Atomic Force Microscopy. *Appl. Phys. Lett.* **2012**, *100*, No. 073106.
4. *Acoustic Scanning Probe Microscopy*; Marinello, F.; Passeri, D., Savio, E., Eds.; Springer: Berlin, 2013.
5. Rabe, U.; Arnold, W. Acoustic Microscopy by Atomic Force Microscopy. *Appl. Phys. Lett.* **1994**, *64*, 1493.
6. Rabe, U. Atomic Force Acoustic Microscopy. In *Applied Scanning Probe Methods II*; Bhushan, B., Fuchs, H., Eds.; Springer: Berlin, 2006; pp 37–90.
7. Yamanaka, K.; Ogiso, H.; Kolosov, O. Ultrasonic Force Microscopy for Nanometer Resolution Subsurface Imaging. *Appl. Phys. Lett.* **1994**, *64*, 178.
8. Yablon, D. G.; Gannepalli, A.; Proksch, R.; Killgore, J.; Hurley, D. C.; Grabowski, J.; Tsou, A. H. Quantitative Viscoelastic Mapping of Polyolefin Blends with Contact Resonance Atomic Force Microscopy. *Macromolecules* **2012**, *45*, 4363–4370.
9. Collins, L.; Tselev, A.; Jesse, S.; Okatan, M. B.; Proksch, R.; Mathews, J. P.; Mitchell, G. D.; Rodriguez, B. J.; Kalinin, S. V.; Ivanov, I. N. Breaking the Limits of Structural and Mechanical Imaging of the Heterogeneous Structure of Coal Macerals. *Nanotechnology* **2014**, *25*, No. 435402.
10. Li, T.; Zeng, K. Nanoscale Elasticity Mappings of Microconstituents of Abalone Shell by Band Excitation-Contact Resonance Force Microscopy. *Nanoscale* **2014**, *6*, 2177–2185.
11. Parlak, Z.; Tu, Q.; Zauscher, S. Liquid Contact Resonance AFM. *Nanotechnology* **2014**, *25*, No. 445703.
12. Umeda, N.; Ishizaki, S.; Uwai, H. Scanning Attractive Force Microscope Using Photothermal Vibration. *J. Vac. Sci. Technol. B* **1991**, *9*, 1318.
13. Ratcliff, G. C.; Erie, D. A.; Superfine, R. Photothermal Modulation for Oscillating Mode Atomic Force Microscopy in Solution. *Appl. Phys. Lett.* **1998**, *72*, 1911.
14. See descriptions on the manufacturer's Web site: Asylum Research, an Oxford Instruments company, <https://www.asylumresearch.com/Products/blueDrive/blueDrive.shtml>.
15. Kocun, M.; Labuda, A.; Gannepalli, A.; Proksch, R. Photothermally Excited Contact Resonance Imaging in Air and Water. *arXiv.org*, **2014**, No. 1410.3311 (<http://arxiv.org/ftp/arxiv/papers/1410/1410.3311.pdf>). This is a concurrent photothermal excitation CR-AFM study, especially about the imaging in liquid.
16. Jesse, S.; Lee, H. N.; Kalinin, S. V. Quantitative Mapping of Switching Behavior in Piezoresponse Force Microscopy. *Rev. Sci. Instrum.* **2006**, *77*, No. 073702.
17. Li, Q.; Liu, Y.; Wang, D.; Withers, R. L.; Li, Z.; Luo, H.; Xu, Z. Switching Spectroscopic Measurement of Surface Potentials on Ferroelectric Surfaces via An Open-Loop Kelvin Probe Force Microscopy Method. *Appl. Phys. Lett.* **2012**, *101*, No. 242906.
18. Balke, N.; Maksymovych, P.; Jesse, S.; Kravchenko, I. I.; Li, Q.; Kalinin, S. V. Exploring Local Electrostatic Effects with Scanning Probe Microscopy: Implications for Piezoresponse Force Microscopy and Triboelectricity. *ACS Nano* **2014**, *8*, 10229–10236.
19. Nikiforov, M. P.; Jesse, S.; Morozovska, A. N.; Eliseev, E. A.; Germinario, L. T.; Kalinin, S. V. Probing the Temperature Dependence of the Mechanical Properties of Polymers at The Nanoscale with Band Excitation Thermal Scanning Probe Microscopy. *Nanotechnology* **2009**, *20*, No. 395705.
20. Jesse, S.; Kalinin, S. V.; Proksch, R.; Baddorf, A.; Rodriguez, B. The Band Excitation Method in Scanning Probe Microscopy for Rapid Mapping of Energy Dissipation on the Nanoscale. *Nanotechnology* **2007**, *18*, No. 435503.
21. Jesse, S.; Kalinin, S. V. Band Excitation in Scanning Probe Microscopy: Sines of Change. *J. Phys. D: Appl. Phys.* **2011**, *44*, No. 464006.
22. Jesse, S.; Vasudevan, R. K.; Collins, L.; Strelcov, E.; Okatan, M. B.; Belianinov, A.; Baddorf, A. P.; Proksch, R.; Kalinin, S. V. Band Excitation in Scanning Probe Microscopy: Recognition and Functional Imaging. *Annu. Rev. Phys. Chem.* **2014**, *65*, 519–536.
23. Arruda, T. M.; Kumar, A.; Jesse, S.; Kalinin, S. V.; Jesse, S. Mapping Irreversible Electrochemical Processes on the Nanoscale: Ionic Phenomena in Li Ion Conductive Glass Ceramics. *Nano Lett.* **2011**, *11*, 4161–4167.
24. Griggio, F.; Jesse, S.; Kumar, A.; Marincel, D. M.; Tinberg, D. S.; Kalinin, S. V.; Trolrier-McKinstry, S. Mapping Piezoelectric Nonlinearity in the Rayleigh Regime Using Band Excitation Piezoresponse Force Microscopy. *Appl. Phys. Lett.* **2011**, *98*, No. 212901.
25. Li, Q.; Liu, Y.; Cheng, Z.; Bian, J.; Chen, H.; Withers, R. L. Observation of Short-Lived Local Polar States Induced by Applied Tip Biases in BaTiO₃-Based Relaxor Ferroelectric Ceramics. *Appl. Phys. Lett.* **2013**, *103*, No. 022904.
26. Rodriguez, B. J.; Callahan, C.; Kalinin, S. V.; Proksch, R. Dual-Frequency Resonance-Tracking Atomic Force Microscopy. *Nanotechnology* **2007**, *18*, No. 475504.
27. Gannepalli, A.; Yablon, D.; Tsou, A.; Proksch, R. Mapping Nanoscale Elasticity and Dissipation Using Dual Frequency Contact Resonance AFM. *Nanotechnology* **2011**, *22*, No. 355705.
28. Hurley, D. C.; Turner, J. A. Measurement of Poisson's Ratio with Contact-Resonance Atomic Force Microscopy. *J. Appl. Phys.* **2007**, *102*, No. 033509.
29. Killgore, J. P.; Yablon, D. G.; Tsou, A. H.; Gannepalli, A.; Yuya, P. A.; Turner, J. A.; Proksch, R.; Hurley, D. C. Viscoelastic Property Mapping with Contact Resonance Force Microscopy. *Langmuir* **2011**, *27*, 13983–13987.
30. Stan, G.; King, S. W.; Cook, R. F. Nanoscale Mapping of Contact Stiffness and Damping by Contact Resonance Atomic Force Microscopy. *Nanotechnology* **2012**, *23*, No. 215703.
31. Muller, M. K.; Geiss, R. H.; Hurley, D. C. Contact Mechanics and Tip Shape in AFM-Based Nanomechanical Measurements. *Ultramicroscopy* **2006**, *106*, 466–474.
32. Duval, F. C.; Wilson, S. A.; Ensell, G.; Evanno, N. M.; Cain, M. G.; Whatmore, R. W. Characterisation of PZT Thin Film Micro-Actuators Using A Silicon Micro-Force Sensor. *Sens. Actuators A* **2006**, *133*, 35–44.
33. Jesse, S.; Baddorf, A. P.; Kalinin, S. V. Switching Spectroscopy Piezoresponse Force Microscopy of Ferroelectric Materials. *Appl. Phys. Lett.* **2006**, *88*, No. 062908.
34. Tsuji, T.; Ogiso, H.; Akedo, J.; Saito, S.; Fukuda, K.; Yamanaka, K. Evaluation of Domain Boundary of Piezo/Ferroelectric Material by Ultrasonic Atomic Force Microscopy. *Jpn. J. Appl. Phys.* **2004**, *43*, 2907–2913.

35. Wojnar, C. S.; le Graverend, J. B.; Kochmann, D. M. Broad-band Control of the Viscoelasticity of Ferroelectrics via Domain Switching. *Appl. Phys. Lett.* **2014**, *105*, No. 162912.
36. Garcia, R.; Calleja, M.; Perez-Murano, F. Local Oxidation of Silicon Surfaces by Dynamic Force Microscopy: Nanofabrication and Water Bridge Formation. *Appl. Phys. Lett.* **1998**, *72*, 2295.
37. Lyuksyutov, S. F.; Paramonov, P. B.; Dolog, I.; Ralich, R. M. Peculiarities of An Anomalous Electronic Current During Atomic Force Microscopy Assisted Nanolithography on N-Type Silicon. *Nanotechnology* **2003**, *14*, No. 716.
38. Garcia, R.; Knoll, A. W.; Riedo, E. Advanced Scanning Probe Lithography. *Nat. Nanotechnol.* **2014**, *9*, 577–587.
39. Yang, N.; Belianinov, A.; Strelcov, E.; Tebano, A.; Foglietti, V.; Castro, D. D.; Schlueter, C.; Lee, T.; Baddorf, A. P.; Balke, N.; *et al.* Effect of Doping on Surface Reactivity and Conduction Mechanism in Samarium-Doped Ceria Thin Films. *ACS Nano* **2014**, *8*, 12494–12501.
40. Arruda, T. M.; Kumar, A.; Jesse, S.; Veith, G. M.; Tselev, A.; Baddorf, A. P.; Balke, N.; Kalinin, S. V. Toward Quantitative Electrochemical Measurements on the Nanoscale by Scanning Probe Microscopy: Environmental and Current Spreading Effects. *ACS Nano* **2013**, *7*, 8175–8182.
41. Kumar, A.; Ciucci, F.; Morozovska, A. N.; Kalinin, S. V.; Jesse, S. Measuring Oxygen Reduction/Evolution Reactions on the Nanoscale. *Nat. Chem.* **2011**, *3*, 707–713.
42. Experimentally, no wear or deterioration of the tip was found, as evidenced by subsequent CR-AFM imaging results obtained on fresh areas.
43. Stan, G.; Cook, R. F. Mapping the Elastic Properties of Granular Au Films by Contact Resonance Atomic Force Microscopy. *Nanotechnology* **2008**, *19*, 235701.